LAWRENCE
LIVERMORE
NATIONAL
LABORATORY

LLNL-CONF-676480

Effects of High Shock Pressures and Pore Morphology
on Hot Spot Mechanisms in HMX

H. K. Springer, C. M. Tarver, S. Bastea

August 20, 2015

19th Biennial APS Conference on Shock Compression of Condensed Matter
Tampa, FL, United States
June 14, 2015 through June 19, 2015

Disclaimer

Effects of high shock pressures and pore morphology on hot spot mechanisms in HMX

H K Springer[1,a)], C M Tarver[1] and S Bastea[1]

[1]*Energetic Materials Center, Lawrence Livermore National Laboratory, Livermore, CA. USA*

[a)]Corresponding author: keo@llnl.gov

Abstract. The shock initiation and detonation behavior of heterogeneous solid explosives is governed by its microstructure and reactive properties. New additive manufacturing techniques offer unprecedented control of explosive microstructures previously impossible, enabling us to develop novel explosives with tailored shock sensitivity and detonation properties. Since microstructure-performance relationships are not well established for explosives, there is little material design guidance for these manufacturing techniques. In this study, we explore the effects of high shock pressures (15-38 GPa) and different pore morphologies on hot spot mechanisms in HMX. HMX is chosen as the model material because we have much of the chemical-thermal-mechanical properties required for pore collapse simulations. Our simulations are performed using the multi-physics arbitrary Lagrangian Eulerian finite element hydrocode, ALE3D, with Cheetah-based models for the unreacted and the product equation-of-states. We use a temperature-dependent specific heat with the unreacted equation-of-state and a temperature-dependent viscosity model to ensure accurate shock temperatures for subsequent chemistry. The Lindemann Law model is used for shock melting in HMX. In contrast to previous pore collapse studies at lower shock pressures (≤10 GPa) in HMX, our calculations show that shock melting occurs above 15 GPa due to higher bulk heating and a prominent elongated ("jet-like") hot spot region forms. The combination of the elongated hot spot region and the higher bulk heating dramatically increases the growth of reactions. Our calculations show that the reaction rate, dF/dt, increases with increasing shock pressure. We decompose the reaction rate into ignition ($(dF/dt)_{ig}$) and growth ($(dF/dt)_{gr}$) phases to better analyze our results. We define $(dF/dt)_{ig}$ to end and $(dF/dt)_{gr}$ to begin just after pore collapse. We find that $(dF/dt)_{gr} > (dF/dt)_{ig}$ for all pressures considered. $(dF/dt)_{gr}$ changes more significantly from 25 to 38 GPa (from 0.05/us to >10-100/us) than from 15 to 25 GPa (from 0.005/us to 0.05/us). There is a three orders-of-magnitude difference in the reaction from 15 to 38 GPa just after pore collapse. This is qualitatively consistent with fitting the (macroscopic) Ignition and Growth model to high pressure shock initiation data, where much larger reaction fractions are needed to capture the early stages of reaction. Calculated burn rates demonstrate better agreement with data at intermediate times in the growth phase for 15 to 25 GPa and late times for 30 GPa then at any time in the growth phase for 38 GPa. Our calculations are much higher than burn rate data at the earliest times in the growth phase for all pressures, which may reflect the higher localized pressures during and just after pore collapse in the ignition phase. Our studies of spherical, conical, and elliptical pore collapse suggest that morphologies accelerating shock initiation at low pressures may not also be dominant at higher pressures approaching steady-state detonation conditions. These studies provide the basis for developing microstructure-aware models that can be used to design new explosives with optimal performance-safety characteristics. Such models can be used to guide additive manufacturing of explosives and fully exploit their disruptive nature.

INTRODUCTION

Shock initiation in heterogeneous solid explosives is primarily governed by hot spot mechanisms since bulk heating alone cannot account for the transition to detonation [1-3]. Experimental observations of detonation failure modes, such as critical diameter and shock desensitization [4-5], also implicates hot spot mechanisms in detonation behavior for much higher pressures. However, it is not clearly understood how pore collapse mechanisms change when the shock pressure increases to near steady-state detonation conditions, e.g., Chapman-Jouguet and von Neumann spike pressures, and with non-spherical pore shapes. The objective of this study is to examine the collapse of single spherical, elliptical, and conical pores in a HMX grain with 15-38 GPa shock pressures. Previous simulation-based studies on single pore collapse in HMX grains have primarily focused on lower shock pressures, spherical pores, and durations too short to probe reaction evolution [6-7]. Recent work has explored non-spherical shapes [8], but these studies were done at lower shock pressures. Higher shock pressures and longer durations have been explored in mesoscale

simulations [9-14] but it is difficult to discern individual pore collapse mechanisms due to the heterogeneous interactions from complex microstructure in these studies. More recent work has improved our understanding of crystal plasticity on pore collapse mechanisms [15], but the results of these studies are not as relevant at higher pressures (>15 GPa) where shock melting reduces the role of strength effects.

MODEL DESCRIPTION

Material Models

We perform 2D axisymmetric pore collapse simulations using the multi-physics arbitrary Lagrangian Eulerian finite element hydrocode, ALE3D [16]. Tabular equation-of-states (EoS) for the unreacted and product HMX are developed using Cheetah [17]. Figure 1 compares our unreacted HMX EoS model along a shock Hugoniot path with experimental data [18-21]. To ensure accurate shock temperatures, we use a temperature-dependent heat capacity model which is fit to the form, $C_V = 9.0\text{x}10^{-4} ln(T) - 4.4\text{x}10^{-3}$, where C_V is in units GPa-cc/g-K and T is temperature in K [22]. Shock melting is captured using the Lindemann Law, which has the form, $T_{melt} = T_{melt,0} exp(2a(1-\nu))(1/\nu)^{2(\gamma_0 - a - 1/3)}$, where ν is the relative volume, $T_{melt,0}$ is the melt temperature at ambient pressure (552K), $\gamma_0 = 1.1$ and $a = 1.66$ [22]. A temperature-dependent viscosity model is also used with the form, $\eta = \eta_0 exp(T_a/T)$, where $\eta_0 = 3.1\text{x}10^{-6}$ Poise and $T_a = 7800K$ [22]. Viscosity model parameters have not been adjusted to account for the pressure-dependent change in HMX melt temperature. For the HMX strength, we use a constant yield and shear modulus of 0.18 and 7.0 GPa, respectively, based on lower bound values in single crystal HMX experiments [23]. A single step Arrhenius kinetic model is used for HMX chemistry with the following parameters: $lnA = 29.35 s^{-1}$, $E_{act} = 35.612$ (kcal/mol) [24]. We use a gamma law gas model for the air in the pore, $P = (\gamma - 1)(\rho/\rho_0)e$, where $\gamma = 1.4$ and e is the energy per reference volume.

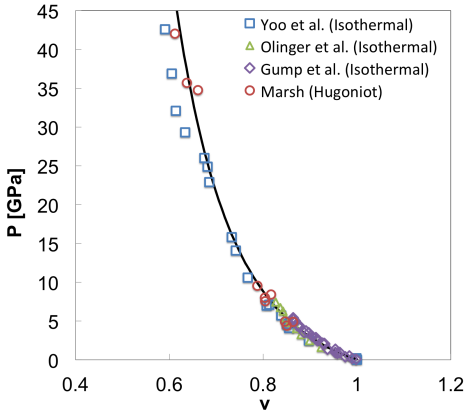

FIGURE 1. Comparison of our Cheetah-based unreacted HMX EoS along a shock Hugoniot path with experimental data [18-21].

Pore Morphology

In this study, we adjust the conical and elliptical pore geometries so that their volumes are equivalent to that of the baseline 1 μm diameter spherical pores. To achieve this for conical pores, the base radius, $r_{base} = r_{sphere}(4R_{cone})^{1/3}$, where r_{sphere} is the spherical pore radius (=0.5 μm) and R_{cone} is the ratio of $r_{base}/h = 0.25, 0.5, 1.0$. For elliptical pores where the long-axis is parallel to the axis of symmetry (prolate spheroid), the minor radius, $r_{minor} = r_{sphere}(R_{ellipse})^{1/3}$, where $R_{ellipse}$ is the ratio of $r_{minor}/r_{major} = 0.25, 0.5$. The cylindrical HMX grain diameter, d_{HMX}, is equal to the HMX grain length, L_{HMX}, and the pore spacing, $l_s = r_{sphere}(16/(3\phi_0))^{1/3}$, where ϕ_0 is the initial porosity. We set $l_s = 25\mu$m, thus HMX grain size, and calculate $\phi_0 = 4.27\text{x}10^{-5}$. ϕ_0, l_s, d_{HMX} and L_{HMX} are fixed in this study.

Figure 2 depicts the general setup for the 2D axisymmetric pore collapse simulations. Prescribed initial velocities are given to the impact region to obtain the desired bulk shock pressures in the HMX grain. The impact and output regions use the unreacted HMX properties to eliminate shock impedance mismatch at the interfaces. In order to capture the reaction evolution over relatively long durations, we employ extended impact and output regions that are $30l_s$ to

circumvent rarefaction waves. The numerical zone size used in this study is 25 nm. In the extended impact and output regions, we use a longitudinal mesh gradient to increase the efficiency of the calculations.

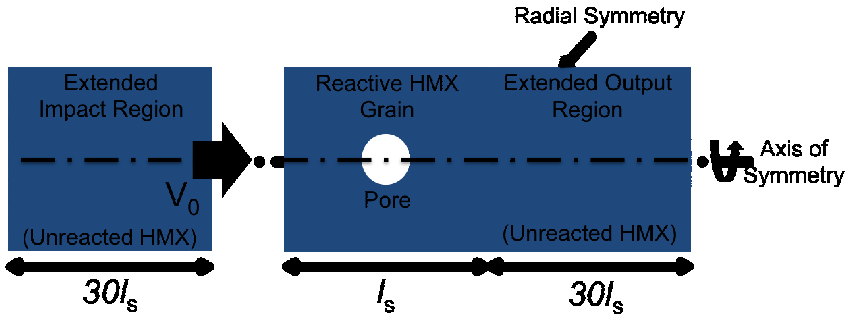

FIGURE 2. General setup for the 2D axisymmetric pore collapse simulations, including the geometry and the boundary conditions.

RESULTS AND DISCUSSION

Figure 3 shows the temperature field in an inert pore collapse simulation for a shock pressure of 25 GPa. The bulk shock heating at this pressure (925K) exceeds the melting point of the HMX, reducing the effects of strength. At 1.1 ns, we observe a relatively round jet tip with a speed of 7.4 km/s which is $> 4U_p$ (particle velocity, $U_p = 1.7km/s$). Jet impact occurs at 1.2 ns and the localized heating exceeds 4000K. The secondary shock from pore collapse emanates outward and is clearly seen at 1.3 ns. By 1.5 ns, the Mach triple point is evident at the junction between the secondary shock and the Mach stem.

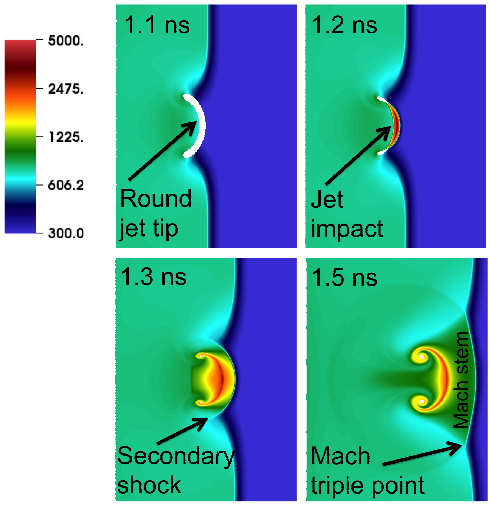

FIGURE 3. Close-up of temperature field (K) in an inert pore collapse simulation for a shock pressure of 25 GPa at 1.1, 1.2, 1.3 and 1.5 ns.

Figure 4 shows the collapse of spherical pores in a reactive HMX grain subjected to shock pressures of 15 and 30 GPa. In order to compare reaction evolution for different pressures, we normalize simulation time by the shock transit time over the HMX grain length ($L_{HMX} = 25\mu$m). The shock transit times for the pressures in this study are: 4.54 ns for 15 GPa, 4.19 ns for 20 GPa, 3.91 ns for 25 GPa, 3.68 ns for 30 GPa, 3.40 ns for 38 GPa. At $t/(L_{HMX}/U_s) = 0.6$, we observe a more protruding jet tip for 30 GPa than for 15 GPa just prior to impact on the distal pore surface. The jet tip speeds for 15 GPa and 30 GPa are 6.5 km/s and 9.1 km/s, respectively, which is more than $4U_p$ for either pressure. At $t/(L_{HMX}/U_s) = 0.72$, the overall reaction progresses much further in the 30 GPa case with the development of a

toroidal-shaped vortex reaction. At $t/(L_{HMX}/U_s) = 1.94$, the reacted regions have now elongated into jets due in part to the kinetic energy of collapse and the release of chemical energy. At the higher pressure, the combination of the more elongated hot spot region and the higher bulk heating dramatically increases the growth of reactions. In fact, the elongated reaction region at 30 GPa serves as a more efficient "line" ignition rather than the traditional concept of a "point" ignition used in analytical spherical pore collapse models [e.g., 25-26].

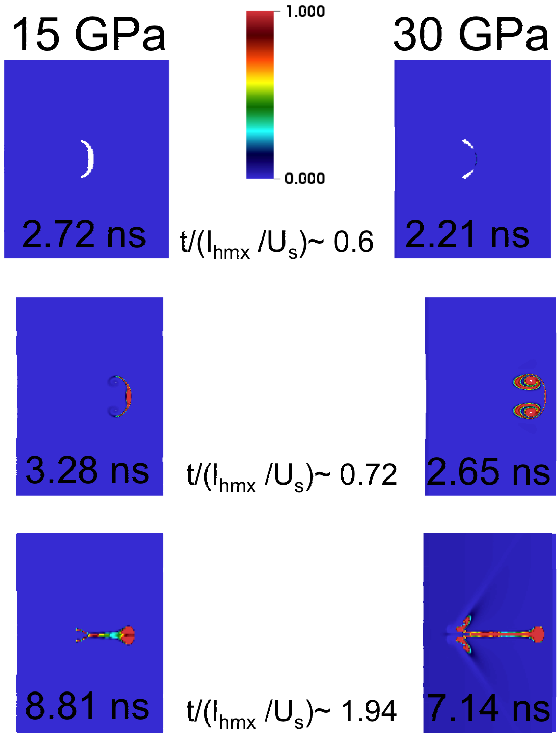

FIGURE 4. Close-up of mass fraction reacted for the collapse of spherical pores subjected to shock pressures of 15 GPa (left) and 30 GPa (right). Simulation and normalized ($t/(L_{HMX}/U_s)$) times are shown on the figure.

Figure 5 shows the reaction rate, dF/dt, and the normalized mass reacted, $M_{reacted}/M_{pore}$, as a function of $t/(L_{HMX}/U_s)$ for spherical pores subjected to pressures of 15, 20, 25, 30, 38 GPa. $M_{reacted}$ is the mass reacted and M_{pore} is the mass of HMX that would fit in the pore similar to Austin et al. [15]. Our calculations show that the reaction rate, dF/dt, increases with increasing shock pressure. We decompose the reaction rate into ignition ($(dF/dt)_{ig}$) and growth ($(dF/dt)_{gr}$) phases to better analyze our results. We define $(dF/dt)_{ig}$ to end and $(dF/dt)_{gr}$ to begin just after pore collapse, at $t/(L_{HMX}/U_s) = 0.5 - 0.6$, where there is a change in reaction rate; this change is more abrupt for 15-25 GPa than for 30-38 GPa. We find that $(dF/dt)_{gr} > (dF/dt)_{ig}$ for all pressures considered. $(dF/dt)_{gr}$ changes more significantly from 25 to 38 GPa (from 0.05/us to >10-100/us) than from 15 to 25 GPa (from 0.005/us to 0.05/us). Higher bulk heating of the HMX grain at 38 GPa and the larger post-collapse hot spot contributes to the accelerated $(dF/dt)_{gr}$. There is a three orders-of-magnitude difference in the reaction from 15 to 38 GPa just after pore collapse. This is qualitatively consistent with fitting the (macroscopic) Ignition and Growth model to high pressure shock initiation data[27], where much larger reaction fractions are needed to capture the early stages of reaction.

In an effort to benchmark our calculations, we derive a simple expression for outward burning of a pore in a HMX grain and compare to conductive burn rate measurements at (static) high pressure conditions [28] in Fig. 6. Our equivalent burn rate is given by, $dr/dt = 144^{-1/3} L_{HMX} F^{-2/3} \dot{F}$, where all parameters are taken from our pore collapse simulations. Experimental measurements range from 32 m/s at 15 GPa to 78 m/s at 38 GPa. Calculated burn rates demonstrate better agreement with data at intermediate times in the growth phase for 15 to 25 GPa and late times for 30 GPa then at any time in the growth phase for 38 GPa. Our calculations are much higher than burn rate data at the earliest times in the growth phase for all pressures, which may reflect the higher localized pressures during and just after pore collapse in the ignition phase.

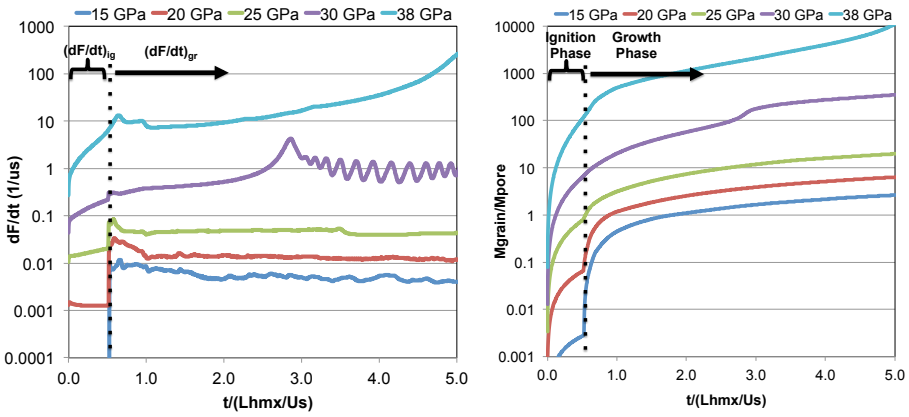

FIGURE 5. Reaction rate, dF/dt, and the normalized mass reacted, $M_{reacted}/M_{pore}$, for spherical pores subjected to pressures of 15, 20, 25, 30, 38 GPa. The reaction rate is decomposed into ignition ($(dF/dt)_{ig}$) and growth ($(dF/dt)_{gr}$) phases.

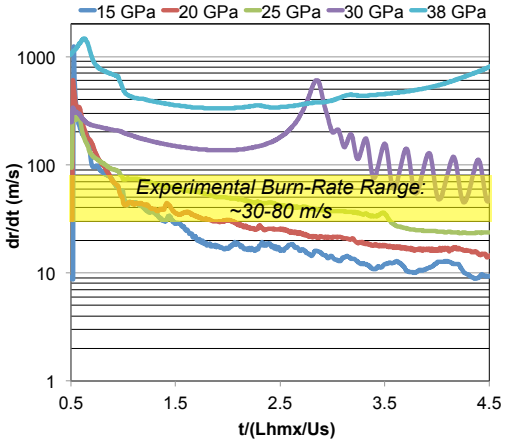

FIGURE 6. Calculated burn rate, $dr/dt = 144^{-1/3} L_{HMX} F^{-2/3} \dot{F}$, at 15, 20, 25, 30, 38 GPa and comparison to experimental measurements of Zaug et al [28].

While the applied shock pressure has a dominant effect on reaction rate, the pore shape also plays an important role. Figure 7 shows the normalized mass reacted, $M_{reacted}/M_{pore}$ versus $t/(L_{HMX}/U_s)$ for spherical, elliptical, and conical pores subjected to pressures of 15 and 30 GPa. At 15 GPa, the highest aspect ratio elliptical ($r_{minor}/r_{major} = 0.25$) and conical ($r_{base}/h = 0.25$) pores are calculated to have the fastest reaction evolution. The conical pores with $r_{base}/h = 0.5, 1.0$ are the next fastest to react and the slowest reaction is for the elliptical pores with $r_{minor}/r_{major} = 0.5$. At 30 GPa, some reordering of the dominant pore shapes occur. The elliptical pore with $r_{minor}/r_{major} = 0.25$ and the conical pore with $r_{base}/h = 0.5$ are still calculated to be the fastest reacting. Though the slowest reacting pore shape at 15 GPa, the elliptical pore with $r_{minor}/r_{major} = 0.5$, is now among the fastest shapes at 30 GPa. While the conical pore with $r_{base}/h = 1.0$, one of the faster reacting shapes at 15 GPa, now becomes the slowest reacting at 30 GPa. Our studies of spherical, conical, and elliptical pore collapse suggest that morphologies accelerating shock initiation at low pressures may not also be dominant at higher pressures approaching steady-state detonation conditions, e.g., Chapman-Jouguet and von Neumann spike pressures.

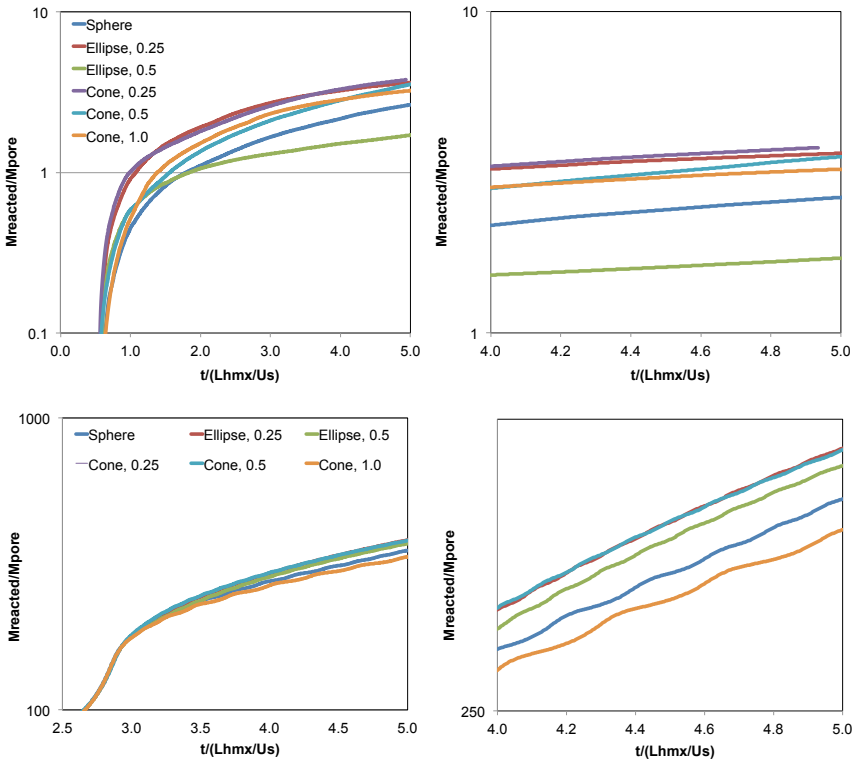

FIGURE 7. $M_{reacted}/M_{pore}$ for spherical, elliptical, and conical pores subjected to pressures of 15 GPa (top) and 30 GPa (bottom). Close-up view provided for $4.0 < t/(L_{HMX}/U_s) < 5.0$ to discern reaction evolution for the different pore shapes.

SUMMARY AND CONCLUSIONS

In this study, we explore the effects of high shock pressures (15-38 GPa) and different pore morphologies on hot spot mechanisms in HMX. In contrast to previous pore collapse studies at lower shock pressures (≤10 GPa) in HMX, our calculations show that shock melting occurs above 15 GPa due to higher bulk heating and a prominent elongated ("jet-like") hot spot region forms. The combination of the elongated hot spot region and the higher bulk heating dramatically increases the growth of reactions. Our calculations show that the reaction rate, dF/dt, increases with increasing shock pressure. We decompose the reaction rate into ignition ($(dF/dt)_{ig}$) and growth ($(dF/dt)_{gr}$) phases to better analyze our results. We define $(dF/dt)_{ig}$ to end and $(dF/dt)_{gr}$ to begin just after pore collapse, at $t/(L_{HMX}/U_s) = 0.5 - 0.6$, where there is a change in reaction rate. We find that $(dF/dt)_{gr} > (dF/dt)_{ig}$ for all pressures considered. $(dF/dt)_{gr}$ changes more significantly from 25 to 38 GPa (from 0.05/us to >10-100/us) than from 15 to 25 GPa (from 0.005/us to 0.05/us). There is a three orders-of-magnitude difference in the reaction from 15 to 38 GPa just after pore collapse. This is qualitatively consistent with fitting the (macroscopic) Ignition and Growth model to high pressure shock initiation data, where much larger reaction fractions are needed to capture the early stages of reaction. Additional calculations are needed at the von Neumann spike pressure to compare to experimentally determined detonation rates for HMX.

In an effort to benchmark our calculations, we derive a simple expression for outward burning of a pore in a HMX grain and compare to conductive burn rate measurements. Calculated burn rates demonstrate better agreement with data at intermediate times in the growth phase for 15 to 25 GPa and late times for 30 GPa then at any time in the growth phase for 38 GPa. Our calculations are much higher than burn rate data at the earliest times in the growth phase for all pressures, which may reflect the higher localized pressures during and just after pore collapse in the ignition phase. Additional experimental validation studies are needed to benchmark our calculations.

Our studies of spherical, conical, and elliptical pore collapse suggest that morphologies accelerating shock initiation at low pressures may not also be dominant at higher pressures approaching steady-state detonation conditions, e.g., Chapman-Jouguet and von Neumann spike pressures.

ACKNOWLEDGMENTS

This work was performed under the auspices of the U.S. DOE by LLNL under Contract DE-AC52-07NA27344. This research was supported by the Joint DoD-DOE Munitions Technology Development Program. LLNL Report LLNL-CONF-676480.

REFERENCES

[1] Bowden F P and Yoffe A D 1952 *Initiation and growth of explosions in liquids and solids* (Cambridge: Cambridge University Press)
[2] Khasainov B A *et al* 1997 On the effect of grain size on shock sensitivity of heterogeneous high explosives *Shock Waves* **7** 89
[3] Mader C L 2008 *Numerical modeling of explosives and propellants, 3rd Ed.* (Boca Raton, FL:CRC Press)
[4] Gibbs T R and Popolato A 1980 *LASL explosive property data* (Berkeley, CA: University of California Press)
[5] Cooper P W 1996 *Explosives engineering* (New York, NY: Wiley-VCH, Inc.)
[6] Menikoff R 2004 Pore collapse and hot spots in HMX *AIP Conf. Proc.* **706** 393
[7] Barton N R *et al* 2009 Defect evolution and pore collapse in crystalline energetic materials *Modeling Simul. Mater. Sci. Eng.* **17** 035003
[8] Levesque G A and Vitello P A 2015 The effect of pore morphology on hot spot temperature *Propellants Explos. Pyrotech.* **40** 303
[9] Baer M R *et al* 1998 Micromechanical modeling of heterogeneous energetic materials *11th Int. Det. Symp.* 788
[10] Baer M R 2002 Modeling heterogeneous energetic materials at the mesoscale *Thermochemica Acta* **384** 351
[11] Reaugh J E 2002 Grain-scale dynamics in explosives *Lawrence Livermore National Laboratory Tech. Rep.* UCRL-ID-150388-2002
[12] Welle E J *et al* 2014 Microstructural effects on the ignition behavior of HMX *AIP Conf. Proc.* **500** 052049-1
[13] Springer H K *et al* 2014 Investigating short-pulse shock initiation in HMX-based explosives with reactive meso-scale simulations *AIP Conf. Proc.* **500** 052041-1
[14] Springer H K *et al* 2015 Investigating shock initiation and detonation in powder HMX with reactive mesoscale simulations *15th Int. Det. Symp.*
[15] Austin R A *et al* 2015 Direct numerical simulation of shear localization and decomposition reactions in shock-loaded HMX crystal *J. Appl. Phys.* **117** 185902
[16] Nichols III A L 2012 ALE3D User's Manual, Version 4.18 *Lawrence Livermore National Laboratory Tech. Rep.* LLNL-SM-604812-2012
[17] Bastea S and Fried L E 2012 Chemical Equillibrium Detonation,*in Shock Wave Science and Technology Reference Library, vol. 6* edited by F. Zhang (New York, NY: Springer)
[18] Olinger B *et al* 1979 The linear and volume compression of β-HMX and RDX to 9 GPa *Proc. Symp. (Int.) on High Dynamic Pressures* 3
[19] Marsh S P 1980 *LASL shock hugoniot data* (Berkeley, CA: University of California Press)
[20] Yoo C-S and Cynn H 1999 Equation of state, phase transition, decomposition of beta-HMX (octahydro-1,3,5,7-tetranitro-1,3,5,7-tetrazocine) at high pressures *J. Chem. Phys.* **111** 10229
[21] Gump J C and Peiris S M 2005 Isothermal equations of state of beta octahydro-1,3,5,7-tetranitro-1,3,5,7-tetrazocine at high temperatures *J. Appl. Phys.* **97** 053513
[22] Menikoff R and Sewell T D 2002 Constituent properties of HMX needed for mesoscale simulations *Combust. Theory Modeling* **6** 103
[23] Menikoff R *et al* 2005 Analysis of wave profiles for single-crystal cyclotetramethylene tetranitramine *J. Appl. Phys.* **97** 023529
[24] Henson B F *et al* 2002 Evidence for thermal equilibrium in the detonation of HMX *12th Int. Det. Symp.* 987
[25] Kang J, Butler P B and Baer M R 1992 A thermomechanical analysis of hot spot formation in condensed-phase, energetic materials *Combustion and Flame* **89** 117
[26] Massoni J *et al* 1998 A mechanistic model for shock initiation of solid explosives *Phys. Fl.* **11** 710
[27] Tarver C M and May C M 2010 Short pulse shock initiation experiments and modeling on LX-16, LX-10, and ultrafine TATB *14th Int. Det. Symp.* 648
[28] Zaug J M *et al* 2010 Deflagration rates of secondary explosives under static MPa-GPa pressure *AIP Conf. Proc.* **1195** 420